

**NON-LINEAR RECONSTRUCTION OF DIELECTRIC TARGET IN  
DISPERSIVE MEDIA FEATURING ULTRA-WIDE BAND SENSING AND  
GRADIENT MINIMIZATION**

**by**

**TAREQ FAISAL ZANOON**

**Thesis submitted in fulfillment of the  
requirements for the degree of  
Doctor of Philosophy**

**June 2011**

## DEDICATION

To my Father, Mother and beloved Family.....

To my Wife, and little daughters “Lara and Sarah”, who little they  
knew why I was facing the computer screen instead of playing  
with them

I dedicate this work .....

## ACKNOWLEDGEMENTS

I must admit that composing these lines is the most difficult throughout this thesis simply because I cannot find the words to express my gratitude to all the people who have given me this opportunity, and made this research possible.

I would like to extend my gratitude to my supervisor, Prof. Mohd Zaid Abdullah who has inspired and accompanied me throughout the stages of this study to the smallest detail. His enthusiastic and continuous support, fruitful discussions, generously infinite time, subjective criticism, and ability to lift spirits at tough times are most precious. Indeed, to me, he was and will still be a part of a dear family. Prof. Zaid, I simply cannot thank you enough. Working with you was an honor.

Special thanks go to the School Electric and Electronic Engineering, USM for providing the necessary facilities and equipment. I acknowledge USM's research Grants 1001.PELECT.814012, 1001.PELECT 811063, as well as the USM fellowship award which made this research financially possible. Special thanks also goes for the School's friendly staff, particularly, En. Amir Hamid and En. Nor Azhar, who offered instant assistance whenever needed. I would also like to thank my colleagues and friends, Sa'eed, Normasniza, Yana, Sa'ad, and my dear friend Motasem, who provided encouragement and precious help.

Finally, if there was anyone in this world who is more happy and proud with this achievement, it would be my dear father, Dr. Faisal Za'noon, who was always been the source of vision, inspiration, generosity, and support, and to whom I will remain to owe the deepest gratitude for the rest of my life. I find myself speechless thanking my mother who bared the years of separation, and shared the dream. I pray for Allah Almighty to have compassion upon them both as they raised me when I was a little child. Sincere word of gratitude goes to my sisters Aman, and Aram, for their endless love, and Sondos, who partially accompanied me through my study period with great patience.

Sincere gratitude also goes to my beloved dear wife, Rashika, who accompanied me throughout this journey, bearing the alienation, and sharing the tough times. Ultimately, as young as they are, as big is my gratitude to my daughters Lara, and Sarah, who bared a busy daddy. You will always be my beloved flourishing roses.

## TABLE OF CONTENTS

	<b>Page</b>
<b>DEDICATION</b> .....	ii
<b>ACKNOWLEDGEMENT</b> .....	iii
<b>TABLE OF CONTENTS</b> .....	v
<b>LIST OF TABLES</b> .....	xiii
<b>LIST OF FIGURES</b> .....	xiv
<b>LIST OF SYMBOLS</b> .....	xxiii
<b>LIST OF ABBREVIATION</b> .....	xxvi
<b>LIST OF PUBLICATIONS</b> .....	xxviii
<b>ABSTRAK</b> .....	xxx
<b>ABSTRACT</b> .....	xxxii

### CHAPTER 1 : INTRODUCTION

1.1 Introduction .....	1
1.2 Ultra-wideband for microwave tomography .....	4
1.3 Difficulties and Challenges .....	6
1.4 Scope and research objectives .....	12
1.5 Thesis outline .....	14

## CHAPTER 2 : REVIEW OF LITERATURE

2.1	Introduction .....	16
2.2	Ionizing and non-ionizing radiation .....	18
2.3	Microwave tomography: Linear and non-linear approaches .....	19
2.3.1	Linear inversion algorithms .....	20
2.3.2	Non-linear inversion algorithms .....	23
2.4	Optimization methods .....	25
2.4.1	Global optimization methods .....	25
2.4.2	Local optimization methods .....	26
2.4.3	Hybrid optimization methods .....	29
2.5	Frequency domain and time domain solutions .....	30
2.5.1	Frequency domain approach .....	31
2.5.2	Frequency hopping approach .....	31
2.5.3	Time domain Approach .....	32
2.6	Tomographic and radar approaches for UWB imaging .....	34
2.6.1	UWB radar imaging .....	34
2.6.1.1	Delay and Sum (DAS) Algorithm .....	35
2.6.1.2	Microwave Imaging via Space-Time beamforming (MIST)	36

2.6.1.3 Tissue sensing adaptive radar (TSAR) .....	37
2.6.2 UWB Tomography .....	38
2.7 UWB imaging Applications .....	42
2.7.1 Medical applications .....	44
2.7.2 Military applications .....	45
2.7.3 Civil applications .....	48
2.7.4 Future trends .....	49
2.8 Summary .....	50

### **CHAPTER 3 : THE FORWARD AND INVERSE SOLVERS**

3.1 Introduction .....	56
3.2 Imaging domain .....	58
3.3 The FDTD method .....	59
3.4 The forward problem .....	61
3.4.1 Descritisation of Maxwell's equations .....	61
3.4.2 One Dimensional descritisation of Maxwell's equations .....	63

3.4.3	Two dimensional descritisation .....	65
3.4.3.1	TE and TM modes .....	65
3.4.3.2	Descritisation of the TM mode .....	66
3.4.4	Determination of step size and stability criteria .....	67
3.4.5	Absorbing boundary and Perfectly Matched Layers (PML) .....	68
3.4.6	Conformal FDTD and modeling of curved geometries .....	73
3.4.7	Modeling of dispersive media .....	75
3.5	The inverse problem .....	80
3.5.1	The cost function .....	81
3.5.2	Gradient of the cost function .....	82
3.5.2.1	The Central Difference and Broyden update approach ...	83
3.5.2.2	The adjoint state method .....	85
3.5.3	Gradient based local minimization methods .....	88
3.5.3.1	The steepest descent .....	89
3.5.3.2	The non-linear conjugate gradient method .....	91
3.6	The inverse problem algorithm .....	93



## CHAPTER 4 : METHODOLOGY

4.1	Introduction .....	100
4.2	Ultra-Wide band source .....	100
4.3	Numerical validation of the discretized Maxwell's equations .....	101
4.3.1	Propagation in one-dimension (1-D) .....	101
4.3.1.1	Free space Propagation in one dimension .....	101
4.3.1.2	Wave interaction with a lossless dielectric .....	103
4.3.1.3	Wave interaction with lossy dielectric .....	105
4.3.2	Propagation in two-Dimension (2-D) .....	107
4.4	Forward and backward time stepping .....	110
4.4.1	Forward time stepping: UWB interaction with a dielectric object .	111
4.4.2	The adjoint solution: backward propagation of residuals .....	114
4.5	Experimental setup .....	115
4.5.1	Data acquisition system .....	116
4.5.2	S-parameters .....	116
4.5.3	UWB Biconical antenna (sensors) .....	118
4.5.4	Vector Network analyzer VNA .....	122

4.5.5 Full view geometry measurements .....	122
4.6 Reconstruction error .....	125

**CHAPTER 5 : EXPERIMENTAL RESULTS – PART I**

5.1 Introduction .....	126
5.2 Sensitivity analysis .....	127
5.2.1 Wave response in homogeneous dispersive media .....	127
5.2.2 Full view geometry .....	131
5.3 Experimental measurements, and validation with the numerical model .	136
5.3.1 Experimental validation in distilled water .....	136
5.3.2 Experimental validation in oil .....	141
5.4 Image reconstruction in simple media .....	144
5.4.1 Influence of priori information on the convergence and optimum solution .....	150
5.4.2 Validation of numerical results with the adjoint state method .....	151
5.5 Image reconstruction from experimental data .....	153
5.5.1 Validation of underwater image reconstruction with the adjoint state method .....	160

## CHAPTER 6 : EXPERIMENTAL RESULTS – PART II

6.1	Introduction .....	162
6.2	Potential and impact of the application .....	163
6.2.1	Limitations of present screening methods .....	164
6.2.2	Tumor size, and stage classification .....	166
6.3	The dielectric properties of the human breast and malignant tumors ....	167
6.4	Breast cancer detection using MRI transformed anatomically realistic data .....	169
6.4.1	Imaging domain .....	169
6.4.2	Anatomically realistic breasts phantom .....	170
6.4.3	Image reconstruction and tumor detection .....	171
6.5	Simulation Experiments .....	174
6.5.1	Numerical model and visualization of tumor growth from numerical data .....	175
6.5.2	Experimental measurements .....	179

6.5.3 Validation of experimental image reconstruction with the adjoint state method .....	182
---	-----

## **CHAPTER 7 : CONCLUSION AND FUTURE WORK**

7.1 Conclusion .....	185
7.2 Suggestions for future work .....	189
7.2.1 Efficiency improvement and parallel processing .....	190
7.2.2 Improving the precision of the acquisition system .....	190
7.2.3 Application to non-homogeneous dielectric profiles .....	191

<b>REFERENCES</b> .....	192
-------------------------	-----

**LIST OF TABLES**

	<b>Page</b>
Table 2.1 Summary of reviewed studies for microwave imaging .....	50
Table 5.1 Numerical domain properties for water and oil models .....	136
Table 6.1 Dielectric properties of female breast tissue .....	168
Table 6.2 Debye parameters and conductivity of dispersive tissue derived from Figures 6.7 and 6.8 .....	176
Table 6.3 Layer structure of materials used in the numerical model .....	177

## LIST OF FIGURES

	<b>Page</b>
Figure 2.1	Ionizing and non-ionizing radiation in the electromagnetic spectrum. 19
Figure 2.2	Effects of increasing the excitation frequency on the signal penetration depth, and non-linearity of the problem ..... 30
Figure 2.3	Frequency hopping from low to high frequencies ..... 32
Figure 2.4	UWB frequency sweep, and corresponding time domain impulse .... 33
Figure 2.5	Illustration of mathematical approaches for microwave imaging ..... 42
Figure 2.6	Lodge's biconical antennas ..... 43
Figure 2.7	Cross section of the human body showing the relative permittivity of various human tissue ..... 44
Figure 2.8	UWB landmine detection systems: (a)1-D antenna array for landmine detection, and (b) Remote controlled vehicle ..... 46
Figure 2.9	UWB through wall imaging radar: (a) system configuration in side-looking mode, (b) orthogonal surveillance paths of the building, (c) combined image obtained from measured data along paths 1 and 2 via back-projection ..... 47
Figure 2.10	UWB radar detection of under rubble live buried people experiment showing: (a) a person in the test position, (b) measurement setup, and (c) breathing pattern ..... 49

Figure 3.1	Input and output parameters of the forward and inverse problems ....	56
Figure 3.2	Topology of the 2-D bounded imaging domain illustrating the imaging plane, and distribution .....	59
Figure 3.3	3D Cartesian Space showing x y z directions .....	62
Figure 3.4	FDTD Interleaving of the electric and magnetic fields in space and time showing the calculation of $H_y^n(k + \frac{1}{2})$ from the previous values of $E_x^{n-\frac{1}{2}}(k)$ and $E_x^{n+\frac{1}{2}}(k)$ . $E_x^{n+\frac{1}{2}}(k + 1)$ is computed following the same manner using $H_y^n(k + \frac{1}{2})$ , and $H_y^n(k + \frac{3}{2})$ .....	65
Figure 3.5	Computational domain showing the structure of the 2-D FDTD grid using PML ABC's .....	69
Figure 3.6	FDTD cell containing mixed materials obtained from the intersection of the FDTD grid and actual curved dielectric .....	74
Figure 3.7	Utilizing the forward and backward time stepping for calculating the gradient .....	88
Figure 3.8	Typical sequence resulting from the method of steepest decent, where $c^k$ is the cost function value at $x^k$ of the $k^{th}$ iteration, and $x^*$ is the minimum .....	90
Figure 3.9	Flow chart of conjugate gradient optimization algorithm using the CDF-Broyden gradient update and Polak-Ribière's modification for non-quadratic solution .....	97

Figure 3.10	Flow chart of conjugate gradient optimization algorithm using the adjoint state method and Polak-Ribière's modification for non-quadratic solution .....	99
Figure 4.1	Gaussian pulses with frequencies (0-1) GHz, (0-3) GHz, and (0-5) GHz: (a) time domain, and (b) frequency domain .....	101
Figure 4.2	Propagation of a (0-3) GHz Gaussian pulse in free space showing electric field $\mathbf{E}_x$ and magnetic field $\mathbf{H}_y$ components at: (a) 58 time steps, (b) 118 time steps, and (c) 158 time steps .....	103
Figure 4.3	Propagation of a (0-3) GHz Gaussian pulse in free space showing electric field $\mathbf{E}_x$ colliding with a lossless dielectric medium of $\epsilon_r=4$ at: (a) 78 time steps, (b) 138 time steps, and (c) 178 time steps .....	104
Figure 4.4	Propagation of a (0-3) GHz Gaussian pulse in free space showing electric field $\mathbf{E}_x$ colliding with a lossy dielectric medium of $\epsilon_r=4$ and $\sigma = 0.05$ S/m at: (a) 78 time steps, (b) 138 time steps, and (c) 178 time steps .....	106
Figure 4.5	Planer (left) and 3-D views (right) of two-Dimensional wave propagation of a (0-3) GHz Gaussian pulse in free space excited at the center of the domain at: (a) 26 time steps, (b) 60 time steps, (c) 120 time steps, and (d) 180 time steps.....	109
Figure 4.6	A point source s emitting electromagnetic radiation equally in all directions passing through the surface of an imaginary sphere of radius r .....	110
Figure 4.7	Planer (left) and 3-D (right) views of 2-dimensional wave propagation of a (0-5) GHz Gaussian pulse in free space at: (a) 70 time steps, (b) 110 time steps, (c) 160 time steps, and (d) 220 time steps corresponding to 0.35 nS, 0.55nS, 0.8ns, and 1.1 nS respectively .....	112



Figure 4.8	Planer (left) and 3-D (right) views of 2-dimensional wave propagation of a (0-5) GHz Gaussian pulse colliding with a dielectric target in free space at: (a) 70 time steps, (b) 110 time steps, (c) 160 time steps, and (d) 220 time steps corresponding to 0.35 nS, 0.55nS, 0.8ns, and 1.1 nS respectively .....	113
Figure 4.9	Adjoint problem when all receivers are excited, captured at (a) 80 time steps, (b) 125 time steps, (c) 160 time steps, and (d) 190 time steps .....	115
Figure 4.10	Schematic of the experimental set-up for UWB imaging .....	116
Figure 4.11	Scattering parameters applied to two port network, showing incident, reflected, and transmitted waves .....	117
Figure 4.12	Typical radiation pattern of omnidirectional antenna showing the elevation and azimuth planes .....	118
Figure 4.13	Biconnical antenna used as sensing element: (a) copper cones, (b) internal structure, and (c) actual antenna .....	120
Figure 4.14	$S_{11}$ response of the assembled antenna measured in the frequency range (9 KHz -8.5 GHz) in water .....	121
Figure 4.15	$S_{11}$ response of the assembled antenna measured in the frequency range (9 KHz-8.5 GHz) in oil .....	122
Figure 4.16	Actual experimental setup with (a) water tank, and (b) oil tank .....	124
Figure 5.1	Full view geometry showing 8 equally distributed s with numbering convention .....	127
Figure 5.2	Permittivity spectrum of distilled water at 20 <sup>o</sup> C .....	128

Figure 5.3	Simulation calculation for observed signals at receivers 2,3,4,5,6,7, and 8 due to the excitation of the first transmitter, in the time range (0-8) ns in water .....	129
Figure 5.4	Recorded simulation of the signal at receiver 5, with transmitter 1 excited, with dispersion (red), without dispersion (blue), and in conductive water (green) in the time range (0-8) ns in water .....	130
Figure 5.5	Simulation calculation for observed signals at receivers 2,3,4,5,6,7, and 8 (left to right ) due to the excitation of the first transmitter, in the time range (0-8) ns in oil .....	131
Figure 5.6	Normalized sensitivity distributions in distilled water corresponding to receivers 2, 3, 4, and 5 denoted by R2, R3, R4, and R5 respectively, in response to exciting transmitter 1: (a) at 1 GHz; (b) at 3 GHz; and (c) at 5 GHz .....	132
Figure 5.7	Isometric view of the sensitivity distributions in distilled water corresponding to receivers 4 (left) and 5 (right) in response to exciting transmitter 1: (a) at 1 GHz; (b) at 3 GHz; and (c) at 5 GHz; with numbering convention similar to figure 5.1 .....	133
Figure 5.8	Normalized sensitivity distributions in oil corresponding to receivers 2, 3, 4, and 5 denoted by R2, R3, R4, and R5 respectively, in response to exciting transmitter 1: (a) at 1 GHz; (b) at 3 GHz; and (c) at 5 GHz .....	134
Figure 5.9	Isometric view of the sensitivity distributions in oil corresponding to receivers 4 (left) and 5 (right) in response to exciting transmitter 1: (a) at 1 GHz; (b) at 3 GHz; and (c) at 5 GHz; with numbering convention similar to Figure 5.1 .....	135
Figure 5.10	Normalized Excitation signal transmitted from antenna 1: Experimental (blue) and approximated Gaussian input (red) .....	137

Figure 5.11	Comparison between modeled and experimental signals in water at receivers 2,3,4, and 5: (a) normalized with respect to the first impulse (b) normalized amplitudes, (c) upper 50% of the modeled signals, and (d) upper 50% of experimental signals after calibration	138
Figure 5.12	Pulse peaks corresponding to the 2-D calculated, and 3-D measured signals, and the correlation with applying the decaying factor associated with the geometrical spreading loss (Rx.2 to Rx8 denote receiver 2 to Receiver 8)	140
Figure 5.13	Comparison between modeled and experimental signals in oil at receivers 2,3,4, and 5: (a) normalized with respect to the first impulse, and (b) normalized amplitudes, (c) upper 50% of the modeled signals, and (d) upper 50% of experimental signals after calibration	143
Figure 5.14	Actual location of the dielectric targets: (a) the letter T, and (b) the scattered targets	144
Figure 5.15	Iterative sequence for reconstructing the T shaped dielectric target showing, (a) the gradient, and (b) the dielectric profile at different iterative steps	147
Figure 5.16	Dielectric profile reconstruction of the T shaped dielectric target showing, (a) actual image, (b) reconstructed image after 18 iterations, and (c) pixel reconstruction error	148
Figure 5.17	Isometric view of the T target showing, (a) actual profile, (b) reconstructed profile, and (c) normalized convergence trend	148
Figure 5.18	Dielectric profile reconstructions of the multiple dielectric targets showing, (a) actual image, (b) reconstructed image after 12 iterations, and (c) pixel reconstruction error	149
Figure 5.19	Isometric view of the multiple dielectric targets showing, (a) actual profile, (b) reconstructed profile, and (c) convergence trend	149

Figure 5.20	Comparison between bounded and unbounded permittivity reconstruction for the T dielectric shape showing, (a) actual, (b) unbounded profile, (c) bounded profile with upper and lower limits, and (d) normalized convergence trend .....	151
Figure 5.21	Comparison of the reconstructed dielectric profiles of the actual image (a) and their pixel reconstruction error using: the adjoint method (b,c), the central difference method (d,e) , and their normalized convergence trend (f) .....	152
Figure 5.22	Recorded experimental measurements in homogeneous media (blue), and with the presence of two test targets (red) at receivers 2, 3, 4, 5, 6,7 and 8 due to the excitation of transmitter 1 .....	155
Figure 5.23	Overall permittivity profile of the solution showing the combination of the dispersive background and unknown variable search region ...	157
Figure 5.24	Image reconstruction from experimental data featuring a 5 mm target showing, (a) actual tubes, (b) designated locations, (c) reconstructed images, and (d) normalized convergence trend .....	158
Figure 5.25	Image reconstruction from experimental data featuring a 10 mm target showing, (a) actual tubes, (b) designated locations, (c) reconstructed images, and (d) normalized convergence trend .....	158
Figure 5.26	Image reconstruction from experimental data featuring two targets of 5 mm and 10 mm in diameter showing, (a) actual tubes, (b) designated locations, (c) reconstructed images, and (d) normalized convergence trend .....	159
Figure 5.27	Image reconstruction from experimental data featuring two targets of 5 mm and 10 mm in diameter showing, (a) adjoint reconstruction, (b) central difference Broyden update, and (c) their corresponding convergence trend .....	160

Figure 6.1	Graphical diagram showing breast tumor size corresponding to: (a) stage T1, (b) stage T2, and (c) stage T3 .....	167
Figure 6.2	T1-MRI (upper) and their corresponding dielectric properties at 5GHz (lower) of breast classification showing, (a) mostly fatty (<25% glandular tissue), (b) scattered fibro-glandular tissue (25-50% glandular), (c) heterogeneously dense breast (51-75% glandular), and (d) very dense breast (>75% glandular) .....	169
Figure 6.3	Realistic MRI derived numerical breast model: (a) sagittal slice, (b) cross section at 5GHz, and (c) cross section with 5 mm tumor .....	171
Figure 6.4	Numerical results for the MRI breast model obtained by: (a) adjoint method, (b) CDF-Broyden update method, and (c) their convergence trend .....	173
Figure 6.5	Experimental breast phantom made from chicken skin and butter; (a) top view, (b) side view .....	175
Figure 6.6	Variation of permittivity as a function of frequency for salted butter (0-3 GHz), and fitted Debye model .....	176
Figure 6.7	Variation of permittivity as a function of frequency for dry skin (0-5 GHz), and fitted Debye model .....	176
Figure 6.8	2-D Permittivity matrix composed by combining individual layers of material .....	177
Figure 6.9	Actual ( upper) and reconstructed (lower) images of the numerical breast phantom constructed from biological materials showing a tumor growth corresponding to: (a) 5 mm (b) 8 mm (c) 13 mm, and (d) 18 mm .....	178
Figure 6.10	Actual image of 5 mm target placed inside the breast phantom prior to sealing .....	179

Figure 6.11	Designated target locations ( upper) and reconstructed (lower) images from the biologically constructed experimental breast phantom, showing tumor growth corresponding to tumor sizes of : (a) 5 mm (b) 10 mm (c) and 15 mm .....	181
Figure 6.12	Iterative reduction in cost function error normalized with respect to the maximum error for the 15 mm, 10 mm, and 5 mm tumor experiments .....	181
Figure 6.13	Experimental results obtained by: (a) adjoint method, and (b) CDF-Broyden update method, and (c) their convergence trend .....	183
Figure 7.1	Realization of 3-D reconstruction from multiple tomographic slices showing, (a) 2-D tomographic slice, and (b) sagittal cross section of the 2-D layers .....	191

## LIST OF SYMBOLS

$\mu_0$	Free Space Permeability
$\mu_r$	Relative Permeability
$\sigma^*$	Electric Conductivity
$N_{PML}$	Number of PML Cells
$c_0$	Propagation Speed in free space
$k_0$	Wave Number
$n^*$	Number of Backward Time Steps
$\epsilon_0$	Free Space Permittivity
$\epsilon_\infty$	Infinite Relative Permittivity
$\epsilon_r$	Relative Permittivity
$\epsilon_r^{eff}$	Effective Relative Permittivity
$\epsilon_s$	Static Relative Permittivity
$h$	Adjoint Magnetic Field
$H$	Characteristic Impedance
$\eta$	Intrinsic Impedance
$\lambda$	Wave Length
$M$	Permeability
$\sigma$	Electric Conductivity

$\tau$	Relaxation Time
$\omega$	Angular frequency
$\Gamma$	Reflection Coefficient
$A$	$A$ is the total cell area
$B$	Magnetic Flux Density
$D$	electric flux density
$E$	Electric Field
$H$	Magnetic Field
$I$	Identity Matrix
$Nt$	Total Number of Time Steps
$Nx$	Total Number of indices Along the X-Axis
$Ny$	Total Number of indices Along the Y-Axis
$T$	Total Scanning Time
$V$	$V$ is the total cell volume
$d$	Adjoint flux density
$e$	Adjoint Electric Field
$g$	Gradient
$i$	Index Number Along the X Axis
$j$	Index Number Along the Y Axis
$k$	Index Number Along the Z Axis



$v$	Propagation speed
$J$	Jacobian
$j$	$\sqrt{-1}$
$k$	Iteration Number
$t$	Reverse time step
$\mathcal{H}$	Hessian Matrix
$\mathcal{J}$	Current Density
$\delta$	Dirac delta function
$\varepsilon$	Permittivity
$\rho$	Charge density
$\omega$	Angular Frequency
$Z$	Characteristic Impedance

## LIST OF ABBREVIATIONS

1-D,2-D, and 3-D	One, Two , and Three Dimensions
ABC's	Absorbing Boundary Conditions
BIM	Born Iterative Method
CDF	Central Difference
CFDTD	Conformal Finite Difference Time Domain
CT	Computed Tomography
DAS	Delay and Sum
DBIM	Distorted Born Iterative Method
ECT	Electrical Capacitance Tomography
EIT	Electrical Impedance Tomography
EM	Electromagnetic
FDTD	Finite Difference Time Domain
FEM	Finite Element Method
GPR	Ground Penetrating Radar
MIST	Microwave Imaging via Space-Time Beamforming
MOM	Method of Moment
MRI	Magnetic Resonance Imaging
PEC	Perfect Electrical Conductor
PML	Perfectly Matched Layer
PRE	Pixel Reconstruction Error
SAR	Synthetic Aperture Radar

T1-MRI	T1-Weighted Magnetic Resonance Imaging
TDR	Time Domain Reflectometer
TE	Transverse Electric
TM	Transverse Magnetic
TNM	Tumor, Node, Metastasis
TSAR	Tissue Sensing Adaptive Radar
UWB	Ultra Wide Band
VNA	Vector Network Analyzer

## LIST OF PUBLICATIONS

### International Journals

ABDULLAH, M. Z., BINAJJAJ, S., ZANOON, T. & PEYTON, A. J. 2010. High-resolution imaging of dielectric profiles by using a time-domain ultra wideband radar sensors. *Elsiever: Measurement*, 44, 859-870.

ZANOON, T. F., and ABDULLAH, M.Z., Quantitative Imaging in the Time Domain Featuring Gradient Based Minimization and Broyden Updating, *IEEE Microwave and Wireless Components Letters*. In Press.

ZANOON, T. F., and ABDULLAH, M.Z., Early stage breast cancer detection by means of time-domain ultra wide band sensing. *Measurement Science and Technology*. In Press.

ZANOON, T. F., BINAJJAJ S. A., and ABDULLAH, M.Z. Ultra wideband imaging in the time domain: experimental validation in the dispersive media, *IET Image Processing*, (Submission in review – October 2010).

### Internatioal Proceedings:

BINAJJAJ, S., ZANOON, T. F. & ABDULLAH, M. Z. Iterative and single-step solutions of multi-offset ultra wide band data in the time domain. *IEEE International Workshop on Imaging Systems and Techniques*, 2009. IST '09., 11-12 May 2009, Shenzhen, China. 324-329.

ZANOON, T., BINAJJAJ, S. & ABDULLAH, M. Z. 2009. Imaging with ultra-wideband sensor: application to underwater inspection of concrete structures. *The 1st AUN/Seed-Net Electrical and Electronics Engineering Regional Conference International Symposium on Multimedia and Communication technology* Bangkok, Thailand.

ZANOON, T. F., BINAJJAJ, S. & ABDULLAH, M. Z. Electromagnetic tomography featuring ultra wide band sensor with conformal finite difference (CFDTD) modeling of dispersive media. *IEEE Symposium on Industrial Electronics & Applications, 2009. ISIEA 2009.*, 4-6 Oct. 2009, Kuala Lumpur, Malaysia. 377-382.

ZANOON, T. F., HATHAL, M. S. & ABDULLAH, M. Z. Comparing image reconstruction algorithms for microwave camera featuring ultra wide band sensor. *IEEE International Workshop on Imaging Systems and Techniques, IST 2011.*, 17-18 Oct. 2011, Penang, Malaysia. 112-117.

### **Award**

**Best recommended paper** “BINAJJAJ, S., ZANOON, T. F. & ABDULLAH, M. Z. Iterative and single-step solutions of multi-offset ultra wide band data in the time domain. *IEEE International Workshop on Imaging Systems and Techniques, 2009. IST '09.*, 11-12 May 2009, Shenzhen, China. 324-329”

# PEMBINAAN SEMULA BUKAN LINEAR SASARAN DIELEKTRIK DALAM MEDIA SERAKAN MENAMPILKAN PENDERIAN JALUR LEBAR-ULTRA DAN PENGURANGAN KECERUNAN.

## ABSTRAK

Dalam dekad yang lalu, kecenderungan minat dalam menggunakan isyarat UWB untuk tomografi gelombang mikro semakin meningkat. Kepelbagaian frekuensi dalam isyarat iluminasi UWB menawarkan kombinasi unik yang membolehkan penyebaran panjang gelombang yang panjang dan pendek, dan seterusnya, pengumpulan lebih banyak maklumat mengenai sasaran. Walaupun secara umumnya gelombang mikro memiliki keutamaan dalam banyak aplikasi pengimejan, algoritma penyongsangan membawa kepada pemulihan profil dielektrik adalah kompleks dan terdedah kepada keadaan bising eksperimen dan alam sekitar. Dalam kajian ini, ujian kebolehlaksanaan UWB gelombang mikro tomografi disiasat bagi pembinaan semula imej kuantitatif. Teknik pembinaan semula berdasarkan imej ulangan yang mudah dan teguh dibangunkan untuk menyesuaikan dengan keadaan bising eksperimen. Teknik ini adalah berdasarkan kaedah kecerunan konjugat dengan pendekatan Polak-Ribière bukan kuadratik, manakala kecerunan diperolehi menggunakan teknik perbezaan pusat dan pengemaskinian strategi Broyden. Kebolehlaksanaan dan ketepatan algoritma penyebaran songsang baru ini dibandingkan dengan kaedah dampingan serta algoritma ke depan dan belakang masa-loncatan. Pembinaan semula imej dilakukan pada data berangka yang disintesis, dan data ujian ukuran diperolehi melalui sistem perolehan data khusus. Keputusan menunjukkan keupayaan super resolusi di mana pengesanan sasaran berskala milimeter bersamaan dengan satu per sepuluh gelombang dari data simulasi,

dan satu perempat daripada panjang gelombang melalui data ujikaji diperolehi dalam struktur yang agak kompleks. Prestasi algoritma yang dicadangkan adalah setanding dengan data simulasi kaedah dampingan bebas hingar, di mana mencapai kurang sedikit kesilapan pembangunan semula imej (2,93% berbanding dengan 3.21% dalam ruang bebas, dan 7.69% berbanding dengan 9.05% di fantom MRI-terterbit payudara). Walau bagaimanapun, apabila data eksperimen digunakan, bukti yang menunjukkan bahawa kaedah kemaskini CDF-Broyden adalah lebih kukuh, di mana artifak yang terdapat di tengah-tengah domain pengimejan dan ketidakaturan geometri sasaran lebih jelas terutamanya apabila saiz sasaran menjadi lebih kecil berbanding dengan panjang gelombang. Sebaliknya, peningkatan prestasi kaedah kemaskini CDF-Broyden datang dengan kos pengiraan intensiti, di mana ia memerlukan 20 minit setiap lelaran berbanding setengah minit untuk kaedah dampingan apabila profil dielektrik struktur payudara manusia dibina semula.

# **NON-LINEAR RECONSTRUCTION OF DIELECTRIC TARGET IN DISPERSIVE MEDIA FEATURING ULTRA-WIDE BAND SENSING AND GRADIENT MINIMIZATION**

## **ABSTRACT**

In the last decade, there has been a growing interest in using UWB signals for microwave tomography. The diversity of frequencies in the illuminating UWB signal offers a unique combination enabling scattering of very long to very short wavelengths, and thus, collecting more information about the target. While microwave in general possesses properties of preference for many imaging applications, inversion algorithms leading to recovery of the dielectric profile are complex in their nature, and vulnerable to noisy experimental conditions and environment. In this study, the experimental feasibility of UWB microwave tomography is investigated for quantitative image reconstruction. A simplified yet robust gradient based iterative image reconstruction technique is developed to adapt to the noisy experimental conditions. The technique is based on the conjugate gradient method with Polak-Ribière's non-quadratic approach, while the gradient is obtained using the central difference technique and Broyden's updating strategy. The feasibility and accuracy of this new inverse scattering algorithm is compared with the adjoint method with forward and reverse time-stepping algorithm. Image reconstruction is performed on synthesized numerical data, and experimental measured data, obtained via a specifically designed data acquisition system. Results indicate the super-resolution capability where the detection of millimeter scaled targets corresponding to one tenth of a wavelength from simulated data, and one quarter of a



wavelength via experimental data were obtained in a relatively complicated structure. The performance of the proposed algorithm was comparable with that of the adjoint method in noise-free simulated data, achieving a slightly less image reconstruction error (2.93% compared to 3.21% in free space, and 7.69% compared to 9.05% in MRI-derived breast phantom). However, when experimental data is used, evidence suggests that the CDF-Broyden update method is more robust, where artefacts appearing at the middle of the imaging domain and distorted target geometry were more obvious as the target size became smaller relative to the wavelength. On the other hand, the enhanced performance of the CDF-Broyden update approach comes at the cost of computational intensity, where it requires 20 minutes per iteration compared to half a minute for the adjoint when the dielectric profiles of human breast structures were reconstructed.

# CHAPTER 1

## INTRODUCTION

### 1.1 Introduction

To the present day understanding of modern physics, electromagnetism is one of the four fundamental forces, which together with the strong nuclear, weak nuclear, and gravitational forces govern our universe (Gubser, 2010, Halpern, 2004). Aside from gravity, ultimately all of the forces that we are familiar with are due to electromagnetic interaction (Newman, 2008). Initially, electricity and magnetism were thought to be two separate forces until James Clerk Maxwell (Maxwell, 1873) combined them into what is known today as Maxwell's equations (Zwiebach, 2009). These equations predict the propagation of electromagnetic waves. In 1886, Heinrich Hertz proved Maxwell's theory by transmitting and receiving electromagnetic signals in the form of electrical sparks. Later in 1901, Guglielmo Marconi performed the famous transatlantic transmission of electrical sparks over a large distance (Nikookar et al., 2009). In fact, both Hertz and Marconi's experiments were based on the transmission of an ultra-wideband signal (UWB) simply because the electrical spark (spark gaps used) naturally generated impulse signals with very wide bandwidth (Molisch et al., 2006).

Electromagnetic waves are classified according to their frequency (or wavelength) forming the electromagnetic wave spectrum. This spectrum includes radio waves, microwaves, infrared, visible light, ultraviolet radiation, X-rays, and gamma rays. Microwaves occupy the spectrum with frequencies between 300 MHz and 300 GHz, and

wavelengths between 1 m and 1 mm respectively. The first major application of microwaves was radar, developed and used during World War II, while modern applications of microwaves relate to radio, television, and communication systems (Hinrikus and Riipulk, 2006). Microwaves have also found their application in medical diagnostic and clinical medicine (Lantis et al., 1998, Semenov, 2009).

Analytical solutions of Maxwell's equations are generally applicable to only a few simple geometrical configurations. Such solutions are difficult or impossible to obtain for practical problems that involve complex geometries (Smith, 1997, Knott et al., 2004). Numerical solutions have gained momentum with the availability of computers after they were considered only of theoretical interest, opening the field of computational electromagnetics and electrodynamics. Numerical solutions are based on the approximation of the continuous space of the analytical problem into a discretized sequence or grid in a numerical model. Several numerical methods can be applied to solve the equations involved in scattering problems. Among the most widely used are the Method of Moment (MoM), Finite element Method (FEM), and Finite Difference Time Domain method (FDTD). The choice of which method to implement mainly depends on the problem.

The explosion of computing power in the last two decades has driven the quest for solving more challenging problems that bypass the solution of the direct or forward problems into inverse problems (Abenius, 2004). From a physical perspective, it is

generally recognized that the differences between forward and inverse problems are related to the concepts of cause and effect (Pastorino, 2010b). The forward solution computes the response of a known incident source when all the physical parameters are known, whereas the inverse solution seeks to identify the physical parameters that lead to a known response from a known source. For example, if the problem is related to a scattering, then the forward solver aims to compute the scattered field, while the inverse solver aims to identify the scatterers from the scattered field. Microwave tomography imaging techniques requires both solvers to identify unknown characteristics of the media under investigation.

In the last decades, intensive research has been carried in microwave tomography techniques towards non-invasive imaging targeting several civil and military applications (Pastorino, 2010b, Bolomey and Pichot, 1990). Recently, there has been a growing interest in microwaves for medical imaging applications due to major safety advantages of non-ionizing radiation exposure (Zastrow et al., 2008a, Fear et al., 2002). The non-ionizing microwave radiation does not cause changes on an atomic and molecular level, and therefore, is much less harmful for biological tissues (Hinrikus and Riipulk, 2006). Instead, microwave tomography exploits the differences in the dielectric properties of various types of biological tissue

## 1.2 Ultra-wideband for microwave tomography

In the late 1970's, Jacobi demonstrated the practical feasibility of using microwaves for biomedical imaging by using water immersed microwave antennas to interrogate biological targets (Jacobi et al., 1979). Soon later, (Larsen and Jacobi, 1979), presented images showing the internal structure of water immersed canine kidney, from measurements of transmission coefficients. The use of water in these experiments reduced the dielectric mismatch between the water and the biological tissues allowing sufficient penetration, while maintaining the spatial resolution of the higher frequency. In general, the spatial resolution improves with shorter wavelengths, but consequently, increases the attenuation of the transmitted energy. The choice of the operating frequency will have to be a compromise between the spatial resolution and loss of signal (Jacobi et al., 1979).

Microwave imaging techniques suffer from lack of sufficient collectable information on the scenario under test (Franceschini et al., 2006). This information can be increased by using multi-view and multi-illumination data acquisition systems. An additional improvement to the image reconstruction capabilities can be achieved by performing measurements at multiple frequencies, rather than a single monochromatic frequency. The natural non-linearity of the inverse scattering image reconstruction process increases with higher contrast of the inhomogeneous media (Chew and Lin, 1995). However, the non-linear effects are less pronounced at lower frequencies as opposed to higher frequencies, and subsequently, the use of high mono-frequency data only drives

the inverse problem into being trapped in a local minima in the optimization process (Chew and Lin, 1995). To improve the reconstruction capabilities while maintaining the spatial resolution offered by higher frequencies, the image reconstructed from low frequency data is used as the initial guess to the higher frequency problem. This strategy of slowly hopping from low to higher frequencies, reduces the non-linear effects, and effectively improves the reconstruction capabilities compared to using high frequency directly (Chew and Lin, 1995, Haddadin and Ebbini, 1998, Franceschini et al., 2006, Pichot et al., 1997). A logical extension to frequency hopping would be achieved by increasing the number of scanning frequencies, resulting in a wide band frequency sweep over the desired range. The problem is alternatively solved in the time domain, since the wideband frequency sweep translates to a time domain impulse, utilizing a single set of measurements, and a single solution for whole frequency range.

The advantage of using ultra-wideband as an illuminating source for microwave imaging arises from the transmission of a very wide bandwidth instead of a single monochromatic signal at single or multiple frequencies. This ensures that the target scatters energy at very long as well as very short wavelengths, which in turn, provides more information about the shape and material structure of the objects (Abdullah et al., 2007b). The low frequency spectrum aids in the linearization of the problem (Chew and Lin, 1995), while the high frequency spectrum maintains the spatial resolution. UWB electromagnetic impulses are attenuated and delayed by the penetrated media according to their dielectric properties, and have proven ability to travel through most dielectric obstacles maintaining a separation between object and background clutter (Abdullah et

al., 2007a). The super resolution capability of UWB means that this technique is able to provide reliable information at resolution smaller than Rayleigh resolution of half-wavelength (Kuroda et al., 2007), reaching  $1/30^{\text{th}}$  of a wavelength as a recent study suggests (Gilmore et al., 2010).

### **1.3 Difficulties and Challenges**

The interest in using microwave frequencies for medical imaging, namely early cancer detection, is driven by major safety advantage, super resolution capability, significant dielectric contrast between normal and malignant tissues, patient convenience, and low operating costs. However, microwave medical imaging is still considered an emerging technique although its preliminary basics were laid out more than 3 decades ago, given the difficulty in obtaining accurate and effective dielectric reconstructions (Pastorino, 2010b, Bolomey and Jofre, 2010). The realization of this imaging technique faces several challenges, mainly related to sophisticated mathematical inversion techniques and experimental data acquisition systems.

The UWB image reconstruction technique requires an iterative solution of the forward problem, in which the electromagnetic wave propagation is calculated as a function of the media's dielectric properties, and the inverse problem in which scattered signals are used to reconstruct the spatial distribution of the imaging domain. The core of the reconstruction techniques is to minimize the cost function error by matching the calculated fields with those obtained from measurements. This implies that the forward

solver must be accurate in predicting the actual measurements, while the data acquisition system is accurate enough to satisfy the assumption made in the numerical model in order to achieve the best match.

Many frequency domain methods, such the Finite Element Method (FEM) and the Method of Moment (MoM) have been used to solve forward problem (Rekanos et al., 1999, Kundu et al., 2008). However, the high frequency wide band excitation pulse of the UWB is more suitable solving in time domain, rather than frequency. The Finite Difference Time Domain Method (FDTD) introduced in 1966 (Kane, 1966) is a very popular approach for its simplicity conceptually, and in terms of implementation. The FDTD method divides the computational domain into Cartesian cubic cells in 3-Dimensions (3-D), or rectangular cells 2-Dimensions (2-D). This imposes a problem for modeling of curved geometries as they have to be approximated using a staircase of rectangular cells. This approximation can be improved by reducing the cell size, eventually increasing the computational demand. A very fine grid is certainly affordable if the problem in hand was simply a single simulation run. However this becomes highly impractical when the forward problem is part of an intensive iterative process. The use of approximating techniques, such as the conformal technique, provides a simple yet accurate approximations of curved boundaries without sacrificing the grid size (Wenhua and Mittra, 2001). This method utilizes the individual electric field component along the edge of the cell containing mixed material properties.



To terminate the computational domain, proper boundary conditions must be set to absorb the departing waves and prevent them from being reflected back to the domain. The Perfectly Matched Layers (PML) is among the most effective methods to terminate the FDTD computational domain (Berenger, 1994).

The dependence of the dielectric properties on frequencies should be carefully considered in the numerical model when using wide band frequency excitation, especially with highly dispersive materials such as biological tissues. The dielectric properties of human tissue at microwave frequencies have been studied in the past where various tissues have been observed to possess varying properties according to their water content and structure (Lazebnik et al., 2007b, Campbell and Land, 1992). The single pole first order Debye model can be accurately used to represent the dispersive properties of biological human tissues (Gabriel et al., 1996c, Winters et al., 2009). This model can also be integrated into the FDTD equations (Sullivan, 2000) to model the presence of human tissues.

In comparison to the forward problem, solving the inverse problem to recover the unknown dielectric distribution of the imaging domain is much more complicated. The difficulty in solving the inverse problem arises from two critical aspects: ill-posedness and non-linearity (Abenius, 2004, Joachimowicz et al., 1991). By definition, a problem is well posed if its solution exists, is unique, and depends continuously on the data (Kirsch, 2011). If one of the previous conditions is not satisfied, the problem becomes

ill-posed. The fulfillment of the first two conditions cannot be guaranteed since the inverse scattering problem has inherently non-unique solution due to the inexact observed field data. The measurements obtained are subject to background noise contamination, inaccuracies due to data acquisition, and incompleteness due to the spatial or frequency limitation (Abenius, 2004). The inexact numerical method approximations can lead to instability, and consequently, failing to satisfy the third condition where small perturbation of the data may result in a large error in the solution. As a result, conditions of solution existence, uniqueness and stability are not ensured at once (Henriksson, 2009). The use of regularization procedures and priori information can replace the ill-posed with a well-posed problem to obtain an approximate solution of the original problem. Prior information is related to known physical characteristics of the media under investigation (Pastorino, 2010b).

The second challenge, which imposes a significant practical difficulty, is the non-linearity of inverse scattering problem. The relationship between the scatterer and corresponding field is highly non-linear due to the multiple scattering effects (Colton and Kress, 1998). This non-linearity increases with stronger scatterers (higher dielectric contrast). Based on this property, image reconstruction approaches can be divided into two classes. The first class ignores the non-linearity by using linear approximations, such as Born and Rytov approximations. Despite its fast reconstruction and computational efficiency, ignoring the non-linear relationship limits the successful solution to qualitative images of low contrast targets, consequently limiting their application. The second class of methods formulates the reconstruction algorithm as an

optimization problem that requires an iterative solution. These methods are mathematically complicated and computationally demanding, but yield a robust and accurate qualitative solution (Kidera, 2007). Quantitative methods are able to inspect strong scatterers since they take into account the non-linear nature of the inverse scattering problem, without the approximations used by qualitative methods, making them more suitable for practical applications such as medical imaging.

According to the optimization technique used, inversion algorithms either seek a local or global minimizer of the error cost function. Local inversion or gradient based methods are computationally less demanding compared to global inversion methods, but their performance mainly depends on the initial guess. Global methods on the other hand are more accurate, robust, and less susceptible to the choice of the initial guess. However, they are very demanding computationally. As a result, local optimization techniques offer a trade-off between the required accuracy, and the computational cost.

Deterministic gradient based algorithms require the calculation of the gradient at every iterative step, updating the optimized solution. The adjoint formulation (Abenius, 2004) computes the gradient by the forward propagation of the wave-field, and backward propagation of the residual waves. This approach has been investigated in linear and non-linear inversion approaches where Lagrange multipliers were used to impose constraints. Both single step and iterative solutions were obtained (Binajjaj, 2010, Abdullah et al., 2010, Binajjaj et al., 2009). Although this method is capable of

producing very good results in ideal noise free environment, it remains very sensitive to noise even with the use of a regularization strategy. It was observed that the slight decrease in signal-to-noise ratio could result in the adjoint fields propagating along the paths which do not intercept the transmitter positions, thus, causing the algorithm to diverge.

The central difference evaluation of the gradients, on the other hand, is a computationally intensive process, especially with greater number of pixels reaching higher resolution. However, good and fast estimate of the gradient is possible by using secant methods for multi-variables from which the Jacobian of the next iterative step can be obtained using the present gradient and solution. The best performing of these methods in practice is the one resulting from Broyden formula (Broyden, 1965, Press, 2007). The use of fast gradient estimation reduces the overall computational cost, thus accelerating the reconstruction.

Gradient based optimization solution for multivariable problems range between steepest descent to Newton methods. The former converges in orthogonal steps as the reduction step is chosen to achieve maximum amount of decrease in the cost function. Newton methods, on the other hand, converge faster by calculating the Hessian matrix. The solution, however, requires inverting the Hessian, and therefore, should be positive definite. Although converging in fewer steps, the computational cost of each step is very high, especially if encountering a singular matrix where regularization and approximate

inversion solution might be needed. An intermediate method in the convergence performance is the conjugate directional method which does not use pre-specified directions, but computes the direction as the algorithm progresses. This method can be applied for non-quadratic problems by using the Polak-Ribière modification formula (Chong and Zak, 2001).

#### **1.4 Scope and research objectives**

This research is part of an UWB microwave imaging research project at the school of Electrical and Electronic Engineering, Universiti Sains Malaysia, lead by Prof. Mohd Zaid Abdullah. Earlier successful studies include the development of an iterative and single-step solutions of inverse scattering problem featuring ultra-wideband sensor (Binajjaj, 2010), where linear and non-linear solutions have been developed and validated for solving the inverse scattering problem. The linear solution was obtained via a Born based single step algorithm, while the non-linear solution achieved by utilizing the adjoint state method with the conjugate gradient minimization. The study utilized the FDTD method to model the propagation of UWB pulses in simple media, featuring numerical validation with data captured in both limited and full view geometries. In both cases, experimental trials were also conducted using the single step algorithm. Nevertheless, the need for a precise data acquisition and a robust reconstruction algorithm were clearly observed, limiting the validation of the non-linear solution to numerically synthesized data.

The presented study aims to achieve additional milestones in this research direction, with the general scope focusing on the experimental feasibility of this imaging technique. To meet this objective, the research is pursued in three main areas: a more precise forward solver that takes into account dispersive media behavior and curved geometrical boundaries, a robust iterative inverse reconstruction technique that is capable of handling experimental data conditions leading to quantitative images, and an improved acquisition system to obtain precision measurements.

Additionally, one of the very promising scenarios in which this imaging technique can be applied is the detection of cancerous lesion within the human breast, given the natural tissue composition, and dielectric variance of tumor properties compared to their surrounding living tissue. Thus, the development of this work pays particular attention to this application, although this imaging modality can be applied for a generality of applications.

Concurrently with this study, ongoing research areas are being conducted and explored within the after mentioned research group, which includes enhanced UWB sensor design, investigation of qualitative methods and new reconstruction algorithms, and exploring new medical imaging potentials in effort of realizing a practical prototype in the near future.

Therefore, this study aims to achieve three specific primary objectives listed as follows:

- i- To model the time domain propagation of UWB pulses in dispersive Debye-media using the finite difference time domain method (FDTD), with conformal modeling of curved geometries, and PML absorbing boundary.
- ii- To construct the UWB experimental data acquisition hardware.
- iii- To derive a quantitative reconstruction algorithm based on Polak-Ribière's conjugate gradient method with Broyden's update scheme.

In realizing the primary objectives, this study aims to achieve the following secondary objectives:

- i- To conduct experimental measurements to verify the simulated results using an UWB phantom.
- ii- To validate the methods and procedures using experimental biologically derived breast phantoms and experimental cancerous tumors.
- iii- To experimentally demonstrate the super-resolution phenomenon of UWB in detecting millimeter sized targets.

## **1.5 Thesis outline**

This thesis is divided into seven chapters. In addition to Chapter One, Chapter Two includes an overview of literature on microwave tomography and some major applications, reconstruction methods, and studies in the field leading to the state of the

art trends. In Chapter Three, the forward and inverse problems are presented, illustrating the theoretical approach and mathematical formulations. Chapter Four demonstrates the methods, materials, and experimental setup utilized in this study, while image reconstruction featuring numerical and experimental data are presented in Chapter Five. Experimental results on the application of this imaging technique for early stage breast cancer detection are presented in Chapter Six. Finally, Chapter Seven concludes the findings of this study, and highlights suggested future work.



## CHAPTER 2

### REVIEW OF LITERATURE

#### 2.1 Introduction

Tomography originates from a two Greek words combination “*tomo*” meaning “slice”, and “*graphein*” meaning “draw” (Buzug, 2008). The term refers to the general class of devices and procedures for producing two dimensional cross-sectional images of a three dimensional object (Leahy et al., 2009). The internal structures are revealed through the use of ionizing or non-ionizing penetrating waves (Xu and Eckerman, 2010) in a non-invasive and non-destructive manner. Ionizing sources include X-ray, while microwaves belong to the class of non-ionizing radiation. With the safety advantage of non-ionizing radiation, the use of microwave frequencies for biomedical imaging has been the scope of interest for several decades, realizing the potential and challenges, and exploring several techniques (Jacobi et al., 1979, Priou and Deficis, 1981, Fear et al., 2002, Zastrow et al., 2008a, Chun et al., 2008).

Over the last few decades, significant progress has been achieved in new and emerging topographic techniques, which in addition to microwave tomography include electrical capacitance tomography (ECT), electrical impedance tomography (EIT), optical tomography, ultrasound tomography, and several others. In the case of ECT, and EIT, the imaging technique relies on capacitance and impedance measurement at low frequencies which enable permittivity and conductivity profile reconstruction respectively. While ECT has been explored for industrial process monitoring, such as

imaging liquid/gas mixture in oil pipelines (Abdul Rahim et al., 2010), EIT has been targeted for medical and industrial applications, exploiting the difference in conductivity and permittivity distribution (York, 2001). Ultrasound tomography relies on using sound waves with a frequency above the audible range of human hearing, typically in the MHz range, and has been extended from medical to industrial applications (Rahiman et al., 2006), while optical tomography rely on light measurements through translucent materials, and is currently being researched towards realizing biomedical applications (Dhawan et al., 2010). A detailed and comprehensive review of these techniques is found in (Williams and Beck, 1995, York, 2001).

The higher frequency range offered by microwave indicates that this technique would produce higher resolution images than those of the lower frequency range measurements mentioned earlier (Voutilainen and et al., 2011), and restriction of semi transparent media. In principle, microwave imaging techniques can be classified to passive, hybrid and active techniques (Hinrikus and Riipulk, 2006, Fear et al., 2002). Passive techniques, known as thermal sensing radiometry, do not use a radiation source, but rather exploits the difference in thermal radiation emitted by targets. Hybrid or microwave-induced acoustic imaging methods use microwaves as an illumination sources, and ultrasound transducers as receivers combining the advantages of microwave stimulation and ultrasound imaging (Lin, 2005, Wang et al., 1999, Kruger et al., 1999). Active microwave technique, for which the work presented here belongs to, uses multiple microwave transmission to interrogate potential targets by measuring their scattered response at several receiving locations. The objective is to recover the

dielectric property profile (or target identification in the case of qualitative methods) from the measured fields on the basis of the difference in dielectric properties of the medium under investigation at microwave frequencies. (Hua et al., 2006, Fear et al., 2003).

## **2.2 Ionizing and non-ionizing radiation**

Radiation sources can be classified either as ionizing or non-ionizing. The distinct properties of both types underline the fundamental difference in the assumptions made for image reconstruction. Ionizing radiation, such as X-rays (Figure 2.1), has high energy to ionize the particles of the substance which they pass through. Additionally, they propagate in straight lines, without suffering from reflection and refraction (Salman et al., 2005). On the other hand, non-ionizing radiation, such as microwaves, does not have enough energy to ionize the penetrated material, thus, raising advantages from the medical perspective as they do not affect the DNA structure (Su et al., 2010, Ptasińska et al., 2008). Nevertheless, there are difficulties associated with using microwave radiation for imaging applications, as they do not follow simple linear paths (Salman et al., 2005, Pan and Kak, 1983). The longer wavelengths of microwaves compared to x-rays makes them susceptible to multiple scattering, refraction, and diffraction effects. As a consequence, the relation between the scatterer and the response of the incident fields becomes inherently non-linear (Marsh et al., 2000, Colton and Kress, 1992, Binajjaj, 2010), requiring solutions that are capable of overcoming the non-linearity, and ill-posedness problems (Abenius, 2004, Joachimowicz et al., 1991).

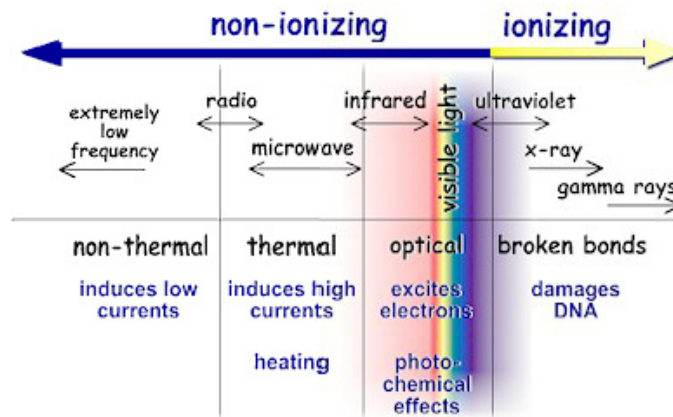


Figure 2.1: Ionizing and non-ionizing radiation in the electromagnetic spectrum (U.S. Environmental Protection Agency, 2011).

### 2.3 Microwave tomography: Linear and non-linear approaches

Pioneering work on the practical feasibility of using microwaves for biomedical imaging came in the late 1970's, when Jacobi and Larsen (Jacobi et al., 1979) used water immersed microwave antennas to interrogate biological targets. Images showing the internal structure of water immersed canine kidney were obtained from measurements of transmission coefficient between two parallel scanning antennas at a monochromatic frequency of 3.9 GHz (Larsen and Jacobi, 1979). In these experiments, the background water medium served as a matching medium between the water and the biological tissues, thus allowing sufficient penetration, while maintaining the spatial resolution of the higher frequency. In later studies, principles of linear path transmission related to X-rays were applied for microwave reconstruction (Ermer et al., 1981, Rao et al., 1980, Maini et al., 1981). Nevertheless, the simplifying assumption fails for strongly inhomogeneous media (Peronnet et al., 1984). In principle, a fundamental difference exists between tomographic imaging with x-rays, and diffracting sources such as microwaves and ultrasounds. The Fourier slice theorem (Mersereau and Oppenheim,

1974), which states that the Fourier transform of a projection is equal to a slice of the two-dimensional Fourier transform of the object, is valid when the projection data measure the line integral of some object parameter along straight lines. This assumption holds for hard-field sources like X-rays (Pan and Kak, 1983). Nevertheless, when the object inhomogeneities are large compared to the wavelength, the propagation is characterized by multipath effects. Reconstruction based on diffraction theorem was presented by Bolomey (Bolomey et al., 1982a), where diffraction effects were taken into account. Peronnet and Bolomey (Bolomey et al., 1982b, Peronnet et al., 1984), also used diffraction tomography to obtain quasi real time images of animal organ using a 3 GHz experimental setup. With the assumption of a weak scatterer, simplified inversions algorithms based on the Born and Raytov approximations were carried out, leading to the application of Fourier Diffraction theorem (Pan and Kak, 1983).

### 2.3.1 Linear inversion algorithms

Early attempts for solving the inverse scattering problems involved making linear approximations of the non-linear problem (Wolf, 1969). Such solutions are valid under certain assumptions that would reduce the non-linearity of the problem, such as the weak scattering assumption. The linearized solution can be obtained by solving the Helmholtz wave equation and utilizing either Born or Raytov approximations to perform the inversion algorithm (Devaney, 1984, Slaney, 1985). Assuming an incident plane wave, the Helmholtz wave equation can be expressed as (Pan and Kak, 1983):

$$(\nabla^2 + k_o^2) u_s(\vec{r}) = -o(\vec{r})u(\vec{r}) \quad (2.1)$$

where  $u(\vec{r})$  is the total field,  $u_s(\vec{r})$  is the scattered fields at point  $r = (x, y, z)$ ,  $o(\vec{r})$  is the object function, and  $k_o = 2\pi/\lambda$ , is the wave number, where  $\lambda$  is the wavelength.

The Helmholtz equation cannot be solved directly, but solution can be written in terms of the Green's function  $g(\vec{r}|\vec{r}')$  (Slaney, 1985, Morse and Feshbach, 1953) such that:

$$u_s(\vec{r}) = \int g(\vec{r} - \vec{r}') o(\vec{r}') u(\vec{r}') d\vec{r}' \quad (2.2)$$

where  $\vec{r}'$  is the point source. For the two dimensional case, the greens function can be expressed as (Kak and Slaney, 2001):

$$g(\vec{r} - \vec{r}') = \pm \frac{j}{4} H_0^{(1)}(k_o R) \quad (2.3)$$

where  $R = |\vec{r} - \vec{r}'|$ , and  $H_0^{(1)}$  is the Hankel function of the first kind. The inverse solution is obtained by solving the object function  $o(\vec{r})$  when both the incident field  $u_i(\vec{r})$ , and the scattered field  $u_s(\vec{r})$  are known. Nevertheless, solving Equation 2.2 is not straight forward due to the non-linear relationship between  $u_s(\vec{r})$  and  $o(\vec{r})$ . The solution may be approximated by using either Born or Raytov approximations. Recalling the total field  $u(\vec{r})$ , the total field at any position can be modeled as the superposition of the incident field and the scattered field (Pan and Kak, 1983):

$$u(\vec{r}) = u_i(\vec{r}) + u_s(\vec{r}) \quad (2.4)$$

and Equation 2.2 can be written as:

$$u_s(\vec{r}) = \int g(\vec{r} - \vec{r}') o(\vec{r}') u_i(\vec{r}') d\vec{r}' + \int g(\vec{r} - \vec{r}') o(\vec{r}') u_s(\vec{r}') d\vec{r}' \quad (2.5)$$

Under the assumption of weak scattering, that is  $u_i(\vec{r}) \gg u_s(\vec{r})$ , the effect of the second integral can be neglected, leading to the Born approximation (Pan and Kak, 1983).

Under this assumption, Equation 2.2 becomes:

$$u_s(\vec{r}) = \int g(\vec{r} - \vec{r}') o(\vec{r}') u_i(\vec{r}') d\vec{r}' \quad (2.6)$$

where the linearized approximation is only valid when the assumption is satisfied.

The Rytov approximation, on the other hand, is based on a slightly different assumption. This approximation is derived by expressing the total complex phase  $\phi(\vec{r})$  as the sum of the incident phase  $\phi_i(\vec{r})$ , and the scattered phase  $\phi_s(\vec{r})$  functions:

$$\phi(\vec{r}) = \phi_i(\vec{r}) + \phi_s(\vec{r}) \quad (2.7)$$

where  $u(\vec{r}) = e^{\phi(\vec{r})}$ . Using this formulation in the wave equation, and following the derivation in (Kak and Slaney, 2001), it can be shown that:

$$(\nabla^2 + k_o^2) u_i \phi_s = -u_i [(\nabla \phi_s)^2 + o(\vec{r})] \quad (2.8)$$

where the function arguments were dropped for simplicity. The solution of this differential equation can be expressed as (Kak and Slaney, 2001):

$$u_i \phi_s = \int_{\nu} g(\vec{r} - \vec{r}') u_i [(\nabla \phi_s)^2 + o(\vec{r}')] d\vec{r}' \quad (2.9)$$

Under the Rytov approximation,  $\nabla \phi_s$  is assumed to be much smaller than  $o(\vec{r})$ , that is:

$$(\nabla \phi_s)^2 + o(\vec{r}) \approx o(\vec{r}) \quad (2.10)$$

Using this approximation, the complex phase of the scattered field is given by (Kak and Slaney, 2001):

$$\phi_s(\vec{r}) = \frac{1}{u_i(\vec{r})} \int_{\nu} g(\vec{r} - \vec{r}') u_i(\vec{r}') o(\vec{r}') d\vec{r}' \quad (2.11)$$

Several studies were dedicated to compare the merit of Born and Rytov approximations under different weak scattering conditions. Nevertheless, as the scattering effects become stronger, the assumptions and approximation of both approaches become violated, limiting the reconstruction capability and applicability. For the detailed derivation and comparative results of both approximations, the reader is referred to (Iwata and Nagata, 1975, Pan and Kak, 1983, Slaney et al., 1984, Salman et al., 2005, Pastorino, 2010b, Rajan and Frisk, 1989, Kak and Slaney, 2001).

The appealing features of the linear approaches lie in the computational efficiency. The consequences of the linearized solutions is that these approaches can only produce qualitative images rather than quantitative, while it is limited to cases of weak scatterers (Binajjaj, 2010, Abdullah et al., 2010). However, in certain applications, retrieving the shape and location of the scatterer is sufficient information, as the values of the objects or background dielectric parameters are unnecessary or obvious (Pastorino, 2010b). An example of this situation is seen in non-destructive testing and quality control, where the shape and location of the defects (such as cracks) are of primary concern.

### **2.3.2 Non-linear inversion algorithms**

As evident from the previous discussion, the natural non-linearity of the inverse scattering problem increases with higher contrast of the inhomogeneous media (Chew and Lin, 1995). The non-linear effects are more pronounced at higher frequencies, subsequently limiting the potential resolution. As a result, non-linear solutions are more



suitable for solving this kind of problem, where the non-linearity of the inverse scattering is retained. The complications, however, lie with the mathematical complexity associated with the solution, and corresponding computational cost due to the iterative procedures. Nevertheless, these types of solutions became feasible in with the advent of the computational power and personal computing in the late 1980's. In comparison with linear approaches, non-linear algorithms are more accurate and robust, making them more appropriate for practical applications, but at a higher computational cost.

In general, non-linear inverse scattering problems are reformulated as an optimization problem that is solved iteratively. Early attempts for solving the non-linearity dates back to the early 1980's (Roger, 1981) where the Newton-Kantorovich algorithm, and regularized Newton methods were investigated. Early studies also explored other optimization techniques such as the conjugate gradient method (Nayanthara et al., 1987). In the early 1990's, Chew and Wang (Wang and Chew, 1989, Chew and Wang, 1990) demonstrated iterative solutions using the iterative Born, and distorted Born iterative methods, obtaining solution in cases when the Born and the Rytov approximations usually break down. An iterative solution based on the Newton-Kantorovich algorithm was also proposed by Joachimowicz et al (Joachimowicz et al., 1991). In his proposed solution, the forward scattering problem was solved using the method of moment, while the initial non-linear relation characterizing the inverse scattering problem was transformed to a sequence of linear ones which minimize the difference between the computed scattered field and the measured scattered field.